

## FOREGROUND REMOVAL BY AN INTERNAL LINEAR COMBINATION METHOD: LIMITATIONS AND IMPLICATIONS

H. K. ERIKSEN<sup>1,2,3</sup>

Institute of Theoretical Astrophysics, University of Oslo, P.O. Box 1029 Blindern,  
N-0315 Oslo, Norway

A. J. BANDAY

Max-Planck-Institut für Astrophysik, Karl-Schwarzschild-Str. 1, Postfach 1317,  
D-85741 Garching bei München, Germany

K. M. GÓRSKI<sup>3,4</sup>

JPL, M/S 169/327, 4800 Oak Grove Drive, Pasadena CA 91109

AND

P. B. LILJE<sup>1</sup>

Institute of Theoretical Astrophysics, University of Oslo, P.O. Box 1029 Blindern,  
N-0315 Oslo, Norway

*Draft version February 7, 2020*

### ABSTRACT

We study the Internal Linear Combination (ILC) method presented by the *WMAP* science team, with the goal of determining whether it may be used for cosmological purposes, as a template-free alternative to existing foreground correction methods. We conclude that the method does have the potential to do just that, but great care must be taken both in implementation, and in a detailed understanding of limitations due to residual foregrounds which can still affect cosmological results. As a first step we demonstrate how to compute the ILC weights both accurately and efficiently by means of Lagrange multipliers, and apply this method to the observed data to produce a new version of the ILC map. This map has 12% lower variance than the official ILC map, primarily due to less noise. Next we describe how to generate Monte Carlo simulations of the ILC map, and find that these agree well with the observed map on angular scales up to  $\ell \approx 200$  on a conservative sky cut. Finally we make two comments to the on-going debates concerning the large-scale properties of the *WMAP* data. First, we note that the Galactic south-eastern quadrant is associated with notably different ILC weights than the other three quadrants, possibly indicating a foreground related anisotropy. Second, we study the properties of the quadrupole and octopole (amplitude, alignment and planarity), and find that residual foregrounds do affect even the largest scales significantly. In particular, we use Monte Carlo simulations to assess the uncertainties connected to these measurements, and find that these are too large to allow for cosmological conclusions at this time.

*Subject headings:* cosmic microwave background — cosmology: observations — methods: numerical

### 1. INTRODUCTION

The first-year release of the *WMAP*<sup>5</sup> data sets (Bennett et al. 2003a) has presented the cosmological community with an extraordinarily rich source of high-quality information, allowing the constraint of specific cosmological models and the parameters which define them to percentage accuracy.

Nevertheless, there remains an important goal beyond such a statistical assessment of the CMB sky, namely

<sup>1</sup> Also at Centre of Mathematics for Applications, University of Oslo, P.O. Box 1053 Blindern, N-0316 Oslo

<sup>2</sup> Also at JPL, M/S 169/327, 4800 Oak Grove Drive, Pasadena CA 91109

<sup>3</sup> Also at California Institute of Technology, Pasadena, CA 91125  
Electronic address: h.k.k.eriksen@astro.uio.no  
Electronic address: banday@MPA-Garching.MPG.DE

<sup>4</sup> Also at Warsaw University Observatory, Aleje Ujazdowskie 4, 00-478 Warszawa, Poland  
Electronic address: Krzysztof.M.Gorski@jpl.nasa.gov

Electronic address: per.lilje@astro.uio.no

<sup>5</sup> The Wilkinson Microwave Anisotropy Probe

to build an accurate image of the last-scattering surface which captures the detailed nature and morphology of our universe, and not simply some best-fit ensemble averaged view of it. Impediments to this program include instrumental noise and systematic artifacts, and foreground emission from local astrophysical objects. On a fundamental level non-cosmological foregrounds can easily compromise any conclusion regarding primordial physics unless properly accounted for, while on a practical level they complicate both algorithms and analyses. Methods for either removing, suppressing or at the very least constraining foregrounds are therefore of great importance, and, indeed, direct attacks on the raw data are very rarely justified. Practically any analysis must consider sky maps which have been processed in some way, either by explicit foreground corrections, or by introducing a sky cut.

The importance of foreground removal has been recognized in the community for a long time (e.g. Banday & Wolfendale 1991; Readhead & Lawrence 1992;

Brandt et al. 1994; Tegmark & Efstathiou 1996; Tegmark 1998; Tegmark et al. 2000), as has the preferred method for discriminating against such contamination, namely multi-frequency observations. While the CMB itself contributes equally to all frequencies (as measured in thermodynamic temperature units) due to the black body nature of its spectrum, foregrounds are typically strongly frequency-dependent. One may therefore distinguish between foregrounds and genuine CMB anisotropy by studying how the signal varies with frequency. However, detailed subtraction of foregrounds has generally required one of two assumptions to be made: either that all of the physical components of the foreground emission and their spectral behavior are known, or that accurate templates of all of the components are available and that the appropriate spectral behavior can be determined by fitting the templates to the available multi-frequency data. Neither method is easily adapted to accommodate real spatial variations in the spectral behavior of the foregrounds.

The *WMAP* project appears to have systematic issues under control, whilst considerable effort has been expended on foreground issues, yet uncertainties may still remain. Recent detections of non-Gaussianity (Chiang et al. 2003; Coles et al. 2003; Eriksen et al. 2004a; Naselsky et al. 2003; Park 2003; Vielva et al. 2003), the continuing debate over the low amplitude of large angular scale anisotropy (see e.g. Efstathiou 2003a, 2003b), and a possible preferred direction or alignment contained therein (de Oliveira-Costa et al. 2003; Eriksen et al. 2004b) may yet be affected by improvements of our ability to remove non-cosmological foregrounds. The *WMAP* satellite observes the sky at five frequencies (23, 33, 41, 61 and 94 GHz), and using at least in part this information the *WMAP* team have applied three different methods for removing, constraining or describing the foregrounds (Bennett et al. 2003b).

The first method is to produce a so-called internal linear combination map (from now on denoted ILC), which assumes nothing about the particular frequency dependencies or morphologies of the foregrounds. Instead, a CMB map is reconstructed by co-adding the data at the five frequencies (now convolved to a common angular resolution of 1 degree) with a set of weights that minimizes the final variance of the map. The details of the non-linear method adopted to derive these weights have not been described by the *WMAP* team. In order to accommodate spectral variability of the foregrounds, the sky has been partitioned into 12 separate regions and the minimum variance criterion applied to each in turn to determine the weights. Discontinuities between regions have been minimized by smoothing of the weights at the boundaries. The resultant CMB map is visually satisfactory but has complex noise properties, and indeed the *WMAP* team *explicitly* warn against its use for cosmological analysis. Nevertheless, the map has been subjected to such studies in the literature, and indeed the *WMAP* team do use the resultant map as an input to their second foreground removal technique.

This involves the application of a Maximum Entropy Method (MEM) in order to construct a model of the foregrounds, component by component. The strength of this method in principle is its ability to reconstruct the synchrotron, free-free and dust emission and their

detailed frequency dependence on a pixel-by-pixel basis. However, the initial stage of the analysis must still utilize templates for these dominant foreground components, and also establishes priors on their spectral behavior by using the *WMAP* data at the five frequencies after correction for a CMB component as determined by the WILC method above. As we will see later, ILC-like methods in general still allow some leakage of foreground signal into the CMB reconstruction, and whether this results in any feedback is difficult to determine. Again as a consequence of complex noise properties, the resultant map has not been considered useful for cosmological purposes. Instead, the *WMAP* team has used the results to interpret the nature of the foreground emission. In particular, they identify a dust-correlated component in the lower frequency (23, 33 and 41 GHz) channels with a spectral index of  $\beta \sim -2.5$  for a spectrum of the form  $\nu^\beta$ . This is physically interpreted as due to a flat spectrum synchrotron component in regions of star formation near the Galactic plane, rather than to emission from spinning dust, which had become the preferred solution to this anomalous, low frequency dust correlated emission. The issue remains open, but recent reanalyses by Lagache (2003) and Finkbeiner (2003) find evidence for the latter interpretation. The origin of this controversy lies simply with the fact that the component separation as implemented by *WMAP* is allowed only to produce a combined synchrotron/spinning dust solution at each frequency, with no attempt made to separately disentangle these two components.

The final method for foreground correction is perhaps the simplest of the three, and it is also the preferred method for generating cleaned maps suitable for cosmological analysis. Rather than inherently exploiting the frequency information contained in the data, one subtracts external templates of the various physical components (i.e. maps produced by non-CMB observations made preferably at frequencies where a specific component dominates the emission) with coupling coefficients determined by cross-correlation to the observed maps. This avoids the noise amplification which occurs when one co-adds the *WMAP* data alone, and has the added benefit that the resultant maps have well-known noise properties, provided that the templates themselves do not contribute significantly to this. Difficulties associated with the method include uncertainties in the detailed morphologies of the templates as scaled to the wavelengths of interest, and the propagation of errors in the coupling coefficients into the error budgets of specific analyses.

It should be noted that Tegmark, de Oliveira-Costa, & Hamilton (2003) have applied a generalization of the ILC method to the *WMAP* data. The basic idea is to allow the weighting of each map to be scale-dependent by performing the analysis in harmonic space, the assumption being that this allows any spatial variations in the spectral dependence of the foregrounds to be adequately tracked. It is not clear to what extent real variations project onto the harmonic eigenmodes of the analysis. As with the WILC method, complex noise properties result, and so it is unlikely that this method is suitable for high precision cosmological analyses. In what follows we will denote the map as TCM – the Tegmark et al. cleaned map.

In this paper we take a new look at the ILC method presented by Bennett et al. (2003b), with the main goal of determining whether a map derived in this manner can be suitable for cosmological purposes. In §2 we start by discussing an alternative algorithm based on Lagrange multipliers for computing the ILC weights. Then, in §3 we show how to generate Monte Carlo simulations of this map, which subsequently are used to study a few efficiency and calibration issues of the method. Next, in §4 we apply the method to the actual *WMAP* data, and produce our own version of the ILC map, which will be called the LILC map – the Lagrange Internal Linear Combination map. The official *WMAP* ILC map will be denoted WILC. Finally, in §5 we consider what consequences this new map may have for the much debated properties of the quadrupole and octopole and their putative alignment, and give a few indications of the uncertainties connected to these results.

## 2. METHOD

We start by reviewing the ideas behind the internal linear combination method as defined by Bennett et al. (2003b), and demonstrate how to compute the ILC weights by means of Lagrange multipliers. This Lagrange multiplier procedure is similar to the approach taken by Tegmark et al. (2003) for computing the harmonic space weights from which their map is constructed. A useful review of this method is also given by Tegmark (1998).

The ILC method is based on a simple premise: suppose there are  $k$  observed CMB maps at different frequencies (but with identical beams), and the aim is to suppress foregrounds and noise as far as possible. Each of the  $k$  maps may be written (in thermodynamic temperature) on the form  $T(\nu_k) = T_{\text{CMB}} + T_{\text{residual}}(\nu_k)$ , where  $T_{\text{CMB}}$  and  $T_{\text{residual}}(\nu_k)$  are statistically independent. Therefore, if we now form the linear combination

$$T = \sum_{i=1}^k w_i T(\nu_i), \quad (1)$$

and require that

$$\sum_{i=1}^k w_i = 1, \quad (2)$$

the resulting map may be written as

$$T = T_{\text{CMB}} + \sum_{i=1}^k w_i T_{\text{residual}}(\nu_i). \quad (3)$$

Thus, the response to the CMB signal is always unity due to its frequency independence, and the  $k - 1$  free weights may be chosen to minimize the impact of the residuals. Assuming the CMB component is statistically independent of the foregrounds and the noise, one convenient measure for this is simply the variance of  $T$ ,

$$\text{Var}(T) = \text{Var}(T_{\text{CMB}}) + \text{Var}\left(\sum_{i=1}^k w_i T_{\text{residual}}(\nu_i)\right). \quad (4)$$

The internal linear combination method may now be defined succinctly in terms of Equations 1 and 2, where the weights are determined by minimizing the variance in Equation 4.

The variance of  $\Delta T$  is nothing but a quadratic form in the weights  $w_i$ , and its minimization under the constraint given in Equation 2 is therefore most conveniently carried out by means of Lagrange multipliers. As shown in Appendix A the linear system of equations to be solved can be written on the following form

$$\begin{bmatrix} \mathbf{B} & -\mathbf{1} \\ \mathbf{1}^T & 0 \end{bmatrix} \begin{bmatrix} \mathbf{w} \\ \lambda \end{bmatrix} = \begin{bmatrix} \mathbf{0} \\ 1 \end{bmatrix}, \quad (5)$$

where  $\lambda$  is an arbitrary constant,  $\mathbf{w} = (w_1, \dots, w_k)^T$  are the ILC weights, and  $\mathbf{t} = (t_1, \dots, t_k)^T$  are the temperature averages over each frequency channel,

$$t_i = \frac{1}{N_{\text{pix}}} \sum_{p=1}^{N_{\text{pix}}} T^i(p), \quad (6)$$

The matrix  $\mathbf{A}$  is defined by

$$A_{ij} = \frac{1}{N_{\text{pix}}} \sum_{p=1}^{N_{\text{pix}}} T^i(p) T^j(p). \quad (7)$$

and, finally, the matrix  $\mathbf{B}$  is

$$B_{ij} = 2(A_{ij} - t_i t_j). \quad (8)$$

If the foreground properties vary strongly over the sky as a result of spatially dependent spectral indexes, then the ILC method may perform rather poorly. To remedy this, one may subdivide the sky into disjoint patches, and compute independent set of weights for each patch. Bennett et al. (2003b) divided the full sky into twelve regions, eleven covering the non-uniform regions of Galactic plane, and the last one covering the Kp2 region plus the well-behaved parts of the Galactic plane. We will study this particular partitioning more closely in §3.

Using such a partitioning, the minimization of the variance in Equation 4 is carried out for each region separately, and the final step is therefore to construct one single full-sky map from those individual patches. In order to suppress boundary effects Bennett et al. (2003b) generated a mask (i.e., a full-sky map consisting of 0's and 1's) for each patch, and convolved these masks by a Gaussian beam of 90' FWHM. The final ILC map was then constructed by first generating one full-sky map from each ILC weight set, as described above, and then they co-added these maps pixel-by-pixel with weights given by the apodized masks. We adopt this method for suppressing boundary effects without modifications.

## 3. SIMULATIONS, CALIBRATION AND PERFORMANCE

Most cosmological CMB analyses are based on Monte Carlo simulations, which in most cases is the only straightforward method of taking into account such real-world nuisances as non-uniformly distributed noise, non-Gaussian beam profiles and complex Galactic cuts. If we want to use the ILC cleaned map for such purposes, we must be able to construct a Monte Carlo ensemble that reproduces the detailed properties of the observed map. In this section, we first discuss how to produce such an ensemble, and then we take advantage of the simulations to study the properties of the ILC method itself.

### 3.1. The simulation pipeline

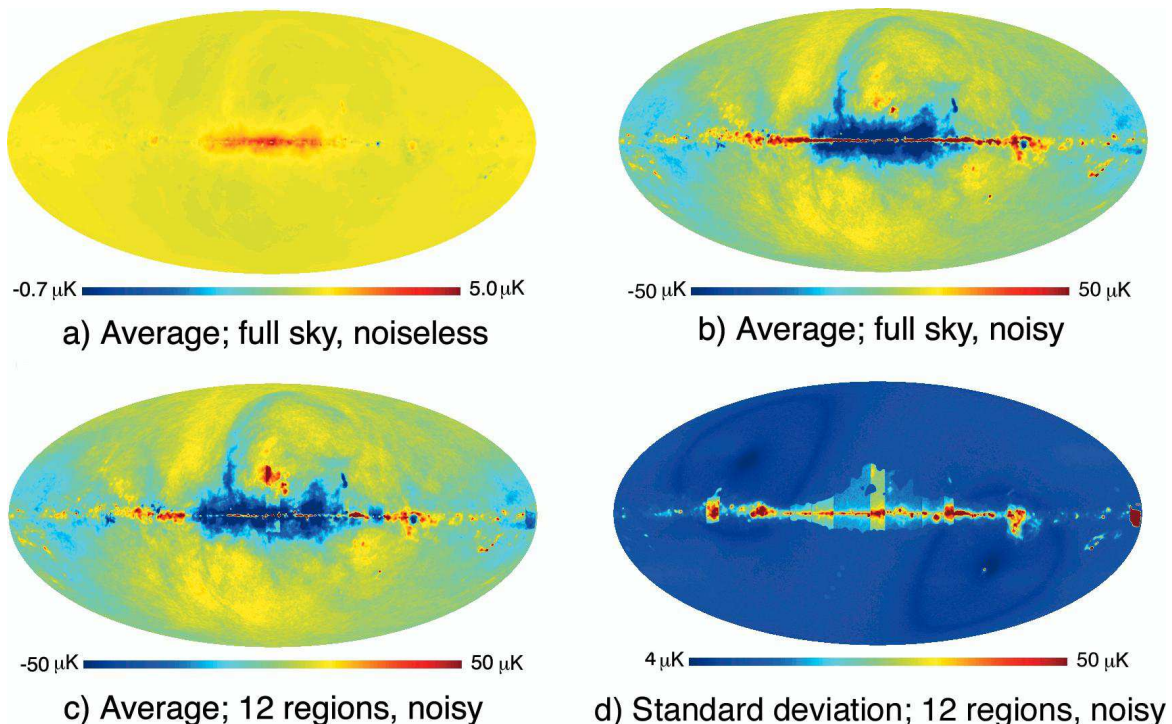


FIG. 1.— Plots showing the pixel-by-pixel average and standard deviation (lower right panel) of the difference maps taken between the reconstructed and the input CMB maps. Each plot is computed from 1000 simulations. *Upper left*: The full sky is treated as one single region, and no noise is added to the simulations. *Upper right*: Same as upper left, but *WMAP* specific noise is included. *Lower left*: The sky is partitioned into the 12 *WMAP* ILC regions, and noise is included. *Lower right*: The standard deviation of the difference maps for which the sky is split into 12 regions, and noise is included.

Monte Carlo simulation of the ILC map amounts simply to producing a set of  $k$  base frequency maps with similar properties to the observed data, which are then processed through the ILC pipeline. The ILC pipeline may then in many respects be regarded simply as one among many statistics we apply to our maps – the crucial part is not the ILC pipeline in itself, but the construction of the base maps. The only difference from main-stream simulation is that we in this case *add* foregrounds to the *simulations*, rather than *subtract* them from the *observations*.

The simulation process may be written in the following algorithmic form<sup>6</sup>:

1. Simulate one CMB component for each realization based on some power spectrum, and convolve this with the appropriate channel-specific beams.
2. Add a channel-specific noise realization.
3. Add channel-specific foreground templates. At this stage the simulation comprises 10 sky maps which mimic the observed properties of the 10 *WMAP* channels at 5 frequency bands.
4. For each channel-specific realization, deconvolve the beam, and convolve to a common resolution corresponding to a Gaussian beam of  $1^\circ$  FWHM.
5. Compute an average map for each frequency.

<sup>6</sup> Although summarized specifically for the *WMAP* processing, the method can clearly be generalized to other multi-frequency experiments.

6. Apply the ILC pipeline.

The only subtle point in this prescription is how to handle foregrounds. Ideally we would like to have a perfect full-sky, noiseless foreground template at each *WMAP* frequency and for each significant foreground (e.g. free-free, synchrotron and dust), but unfortunately, no such templates are available. We are therefore left with several options.

First, we may use the Finkbeiner and Haslam templates (Haslam et al. 1982; Finkbeiner 2003; Finkbeiner et al. 1999) for synchrotron, free-free and dust emission<sup>7</sup>, together with the channel specific weights listed in Table 3 of Bennett et al. (2003b). The channel specific weights are estimated through direct fits to the observed data, and are therefore free of any assumptions about the spectral parameters. Moreover, this method includes the contribution from the anomalous dust-correlated foreground, without the necessity to resolve the spinning dust controversy. In practice, the weighted sum over the three templates approximates the correct amplitudes very well.

On the other hand, at low Galactic latitudes the templates approximate the real sky very poorly due to the complexity of the foreground emission and real spectral variations close to the Galactic plane, thus if a full-sky simulation is required, they should not be trusted. Nevertheless, for the purposes of calibration of our method, such inaccuracies are unlikely to bias our conclusions. Moreover, as we will demonstrate, in this implementa-

<sup>7</sup> Versions of these maps as used in the *WMAP* analysis are available at <http://lambda.gsfc.nasa.gov>.

tion of the ILC method the inner Galactic region will *always* be strongly polluted by foregrounds, and should not be used for cosmological analysis.

A second option is to use the MEM maps provided by the *WMAP* team. The advantage of this method is a much better approximation to the true sky emission at low Galactic latitudes. Unfortunately, these maps are intrinsically noisy, and one would therefore have to compensate for this when adding noise to the simulations. As a result, we adopt the simple template method in this paper, which results in simulations having acceptable power spectra in the high-latitude region. In fact, the simulations are visually acceptable even in the inner Galactic region, having features very much resembling those seen in the observed ILC map.

### 3.2. Sensitivity and response to noise and region definitions

While the ILC method itself is simple to define, it is less clear how accurately it allows the removal of Galactic foreground emission. To quantify this, we utilize our simulation set containing constant and known levels of these foregrounds, reconstruct the CMB sky estimate for each simulation via the ILC method, and compare this to the input CMB component.

For the initial comparison, we consider the idealized case of a full-sky noise-less analysis, including only foregrounds. The results from this exercise are shown in the upper left panel of Figure 1 in terms of the average residual map computed from 1000 simulations. In this case the ILC method does an excellent job of removing the foregrounds, as the residuals are less than  $10 \mu\text{K}$  even in the central Galactic plane. The upper right panel shows the results from a similar full-sky simulation, but for which Gaussian, non-uniform noise has been added to each realization. The effect is striking, indeed, as both the Galactic plane and the North Galactic Spur are now clearly visible. The explanation lies of course in the definition of the ILC method – the ILC weights are defined to minimize the variance of the output map. In the noiseless case, this is an optimization only with respect to the foreground templates; for three templates, no variations in the spectral indices, and four free weights to adjust, this can be performed to high precision. However, the problem becomes more complicated with the introduction of noise, since the minimum variance criterion then implies a trade-off between instrument or foreground noise. As is seen in Figure 1, a higher level of foregrounds in a relatively small region of the sky is preferred over increased noise over the full sky.

Obviously even the clean, high-latitude regions of the sky become polluted by this higher level of foregrounds near the Galactic plane when treating the full sky as one region. In order to avoid such spreading one may therefore choose to divide the sky into separate patches, each with rather homogeneous foreground properties, as described above. While this procedure works very well in practice, there are certain problems that one should be aware of.

In the lower two panels of Figure 1 we have plotted the average (lower left panel) and standard deviation (lower right panel) of the residual maps, when the sky is divided into the 12 regions defined by the *WMAP* team. Overall the average map looks quite similar to the full-sky case,

although the absolute differences are slightly smaller, indicating that the division did in fact have a positive effect. The reason the improvement is relatively small, is because the spectral indexes of the simulations are constant; for the real data, which have varying spectral indexes, the difference between a full-sky and a region-wise treatment is much larger.

However, the two most interesting points in this respect are to be found in the lower right plot, which shows the standard deviation of the difference maps. First, the scanning pattern of *WMAP* is clearly visible in the high-latitude region. This indicates that noise is more important than foregrounds in this region, and therefore the ILC method prefers to minimize this, rather than for instance suppressing the North Galactic Spur, which is clearly visible in the average plot. Secondly, region number 12 (to the very right in the plot) is associated with a very large variance and so the estimated CMB signal is not only biased in this region, but for all practical purposes unknown. In fact, in a number of noiseless simulations we have carried out the ILC weight matrix is singular in this region, indicating that there is simply too little information present here to recover the CMB signal. When adding noise the matrix becomes non-singular, and the procedure does yield a result, but the reconstructed field is likely to be a very poor approximation to the underlying CMB field. The important lesson to be drawn from this is that the size of the patches must be large enough to provide adequate support for CMB reconstruction. Region number 12 is too small to do this, and should therefore either be merged into the large high-latitude region, or extended.

### 3.3. Efficiency considerations

By assuming a fixed spectral index for each of the important foregrounds it is possible to obtain reasonable estimates of the residual foreground level in the ILC map. Suppose each significant foreground may be written in the form  $T_f(\nu) = (\nu/\nu_0)^\beta S_0$  (Bennett et al. 2003b), where  $\nu_0$  is an arbitrary reference frequency for the particular foreground,  $S_0$  is the true foreground distribution on the sky at that frequency,  $\beta$  is the spectral index and  $T$  is measured in antenna temperature. Then the residual foreground contribution to the ILC map may be written on the form

$$T_{\text{residual}} = \left[ \sum_{i=1}^k w_i \left( \frac{\nu_i}{\nu_0} \right)^\beta a(\nu_i) \right] S_0 = f \cdot S_0, \quad (9)$$

where  $a(\nu)$  is the conversion factor from antenna to thermodynamic temperature. Thus, the parameter  $f$  is simply the fraction of residual foregrounds of that particular type in the ILC map, relative to the chosen reference frequency.

For the simulations, we know both the exact CMB component and the noise contributions, and so we can also compute the CMB signal to noise ratio by taking the ratio of the rms of the input CMB component to the noise rms. The latter quantity is computed as follows

$$\sigma_{\text{noise}}^2 = \sum_{i=1}^k w_i^2 \sigma_{\text{noise},i}^2, \quad (10)$$

where  $\sigma_{\text{noise},i}^2$  is the variance of the  $i$ th input noise realization, which we know.

TABLE 1. EFFICIENCY AS A FUNCTION OF REGION

Region	$f_s$	$f_{ff}$	$f_d$	$\frac{\sigma_{\text{CMB}}}{\sigma_{\text{noise}}}$
Full Kp0 region	$0.02 \pm 0.06$	$0.20 \pm 0.13$	$0.54 \pm 0.06$	$6.2 \pm 0.5$
Full Kp2 region	$-0.01 \pm 0.04$	$0.15 \pm 0.09$	$0.54 \pm 0.06$	$6.0 \pm 0.4$
Full Kp4 region	$-0.01 \pm 0.03$	$0.14 \pm 0.07$	$0.55 \pm 0.07$	$5.9 \pm 0.3$
<i>WMAP</i> ILC Kp2	$-0.04 \pm 0.01$	$0.08 \pm 0.03$	$0.55 \pm 0.06$	$5.6 \pm 0.2$
Full sky	$-0.03 \pm 0.01$	$0.10 \pm 0.02$	$0.46 \pm 0.03$	$5.2 \pm 0.2$

NOTE. — The residual foreground levels and signal-to-noise ratios as a function of region size.  $f_s$  – synchrotron fraction relative to the canonical contribution at 22.8 GHz;  $f_{ff}$  – the free-free fraction relative to 33 GHz;  $f_d$  – the dust fraction relative to 93.5 GHz. The numbers are computed from sets of 1000 Monte Carlo simulations.

The efficiency of the ILC method may now be quantified by computing these parameters from the Monte Carlo simulations. Such results are summarized in Table 1 for five different high-latitude regions (including different amount of foregrounds). For each quantity we list the mean and standard deviation, as computed from a set of 1000 simulations. Three foregrounds are included here, namely synchrotron ( $\beta_s = -2.70$ ,  $\nu_{0,s} = 22.8$  GHz), free-free ( $\beta_{ff} = -2.15$ ,  $\nu_{0,ff} = 33.0$  GHz) and thermal dust ( $\beta_d = +2.20$ ,  $\nu_{0,d} = 93.5$  GHz).

The most interesting conclusions to be drawn from this table are the following: First, the ILC method performs quite well with respect to synchrotron emission, independently of the particular sky cut. Second, the more area is included in the analysis, the better it does for free-free emission, implying that the main support for information on free-free lies close to the Galactic plane, which is a reasonable result.

Third, the ILC method performs quite badly with respect to dust – the residual amount of dust in the simulations is approximately half that of the W-band, a point which must be well understood when using the ILC map for foreground studies. We will return to this issue in the next section.

Finally, we see that the signal-to-noise ratio increases when excluding more of the Galactic plane. This is again a manifestation of the competition between noise and foreground reduction. When less foregrounds are included in the region of interest, relatively more emphasis is put on the noise. Thus, one can easily find, somewhat paradoxically, that by manually excluding foreground contaminated regions from the analysis, the final amount of residual foregrounds increases, simply because the area of choice does not carry enough information to calibrate the ILC weights properly, and therefore the ILC method preferentially eliminates noise rather than foregrounds.

#### 4. APPLICATION TO THE *WMAP* DATA

Table 2 lists the ILC weights for each region and for each frequency band, both as computed by Bennett et al. (2003b) and by the Lagrange multiplier method. Figure 2 shows our version of the ILC map.

A comparison of the two weight sets in Table 2 shows clearly that the differences between the two methods are significant. The corresponding effect on the sky of these different weights is shown in Figure 3(a), where the difference between our map and the WILC map is plotted. The most notable features include the large blue area around the Galactic bulge, presumably indicating the different abilities of the two methods to reject some large-scale foreground structures, and secondly the resid-

ual small-scale structure most likely indicating the different noise properties of the two maps.

In Figure 3(b) the difference between our map and the TCM is plotted (the TCM map was convolved to a common resolution of  $1^\circ$  FWHM before computing the difference). There are no noticeable small-scale structures uniformly distributed on the sky, indicating similar noise properties between the two maps. However, there are larger scale residual foreground features present. Some point-source-like residuals are also present, which are associated with known *WMAP* sources. By visual comparison of the TCM and the LILC maps one clearly sees that these residual point sources are present in the former and not in the latter, and therefore the pixel space based ILC method does seem to perform better with respect to point sources than the harmonic space method used by Tegmark et al. (2003).

In order to assess the potential impact of point sources on our method further, we computed weights for the Kp2 region, both including and excluding the 700 point sources resolved by *WMAP*. The effect is negligible, at most a one or two percent modification of the weights. Nevertheless, this comparison does serve to remind us that there will likely be point source residuals in any ILC-derived CMB map.

Another picture of the same comparisons is given in Figure 4. Here we have plotted the full-sky power spectrum of the WILC map, the LILC map and the TCM, together with the best-fit running index spectrum. Clearly, our map agrees very well with the TCM up to about  $\ell = 200$ , but diverges at smaller scales, where the effect of the TCM's narrower W-band beam becomes clearer. The WILC map, however, departs from the other two already at  $\ell \approx 30$ , a difference which is most naturally interpreted as resulting from different noise properties.

Let us now for a moment return to simulations, and compare the observed LILC power spectrum to simulated spectra. Figure 5 shows the power spectrum of the observed ILC map together with 1 and  $2\sigma$  confidence band computed from 1000 simulations; the spectrum in the left panel is computed from the full sky, whereas the conservative Kp0 mask has been imposed in the right panel so that what is shown is actually a pseudo-spectrum. In the full-sky case, we see that the observed spectrum matches the simulations very well up to about  $\ell \approx 100$ , but rises more rapidly from about  $\ell > 150$ . When constrained to the Kp0 region, the observed spectrum follows the simulations all the way up to  $\ell = 200$ , after which a very small bias toward high values may be seen. Thus, the simulations seem to approximate the real sky satisfactory on

TABLE 2. THE WILC AND LILC WEIGHTS

Region	Map	K-band	Ka-band	Q-band	V-band	W-band
1	WILC	0.10876	-0.68367	-0.09579	1.92141	-0.25072
	LILC	-0.19401	0.14004	0.07702	0.61214	0.36480
2	WILC	0.10818	-0.67987	-0.09017	1.96859	-0.30674
	LILC	-0.06280	-0.14738	-0.13982	1.31073	0.03927
3	WILC	-0.04074	-0.28682	0.08476	1.16221	0.08061
	LILC	-0.11470	0.15098	-0.38520	1.16396	0.18496
4	WILC	-0.01847	-0.25533	-0.02607	0.83919	0.46068
	LILC	-0.05654	-0.01464	-0.31223	0.93407	0.44934
5	WILC	0.18610	-0.77416	-0.32352	2.33978	-0.42820
	LILC	0.20099	-0.86252	-0.27825	2.39309	-0.45330
6	WILC	-0.02158	-0.21880	-0.08224	0.84851	0.47412
	LILC	-0.10223	0.21569	-0.51767	0.90277	0.50144
7	WILC	0.11790	-0.67740	-0.09117	1.94830	-0.29763
	LILC	-0.05637	-0.00015	-0.45602	1.46095	0.05159
8	WILC	0.12403	-0.67639	-0.09653	1.74992	-0.10103
	LILC	0.16494	-0.89662	0.07743	2.01377	-0.35952
9	WILC	0.10500	-0.68438	-0.09847	1.90588	-0.22803
	LILC	-0.04577	-0.27660	-0.02097	1.28849	0.05484
10	WILC	0.16911	-0.91455	-0.01204	2.64536	-0.88788
	LILC	0.19380	-1.16103	0.37899	2.26627	-0.67803
11	WILC	0.21951	-0.96567	-0.18077	2.38740	-0.46046
	LILC	0.22200	-1.03357	-0.09824	2.34490	-0.43509
12	WILC	0.11101	-0.67501	0.05268	1.59101	-0.07970
	LILC	-0.06397	-0.00907	-0.46855	1.92500	-0.38342

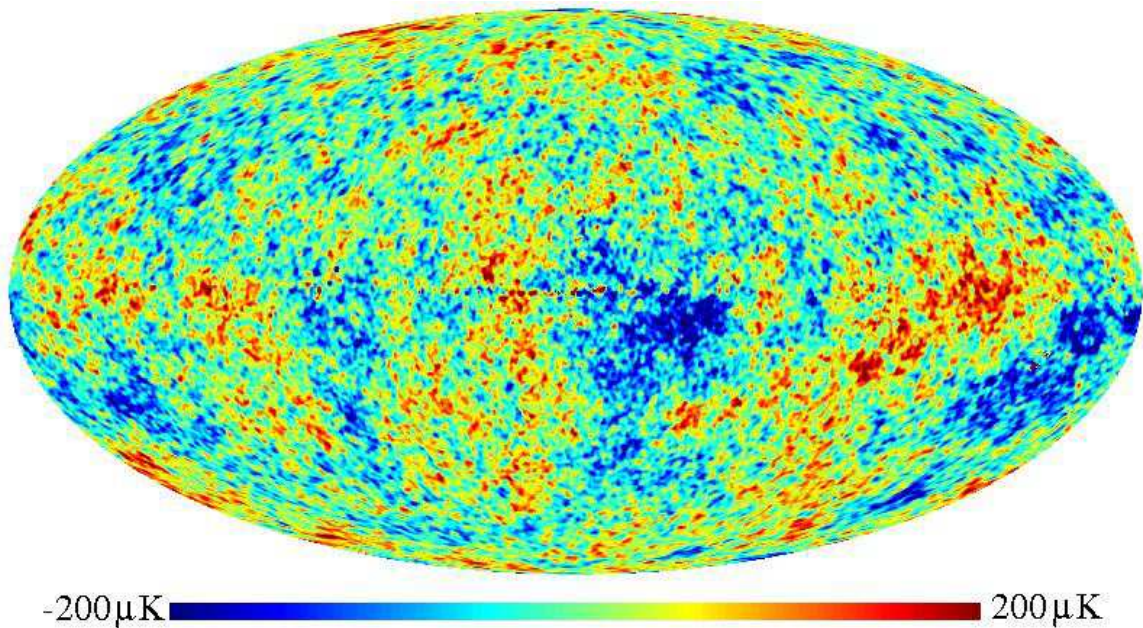
NOTE. — Comparison of the official *WMAP* ILC weights and the Lagrange multiplier weights as derived in this paper.

FIG. 2.— The Lagrange Internal Linear Combination (LILC) map.

the Kp0 region, while they underestimate the level of residual foregrounds in the inner Galactic regions.

The defining criterion of the ILC method is of course minimum variance, and the rms of the high-latitude region of the LILC is  $68 \mu\text{K}$ , while the corresponding num-

ber for the WILC is  $72 \mu\text{K}$ . In other words, our set of weights results in 12% lower variance, and is therefore better as far as the minimum variance definition is concerned. However, this does not necessarily mean that the level of residual foregrounds is smaller. In this, the

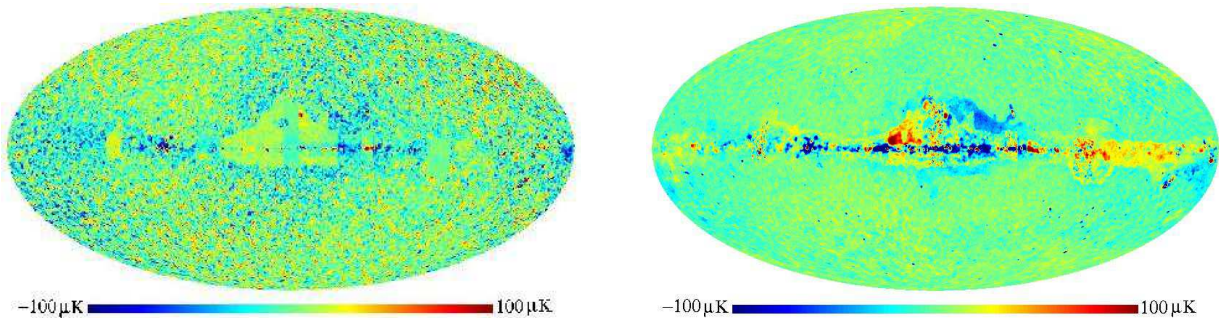


FIG. 3.— The difference between the LILC map and a) the WILC map and b) the TCM. The monopole and dipole were removed from the former map, and the latter was smoothed to  $1^\circ$  FWHM before differencing.

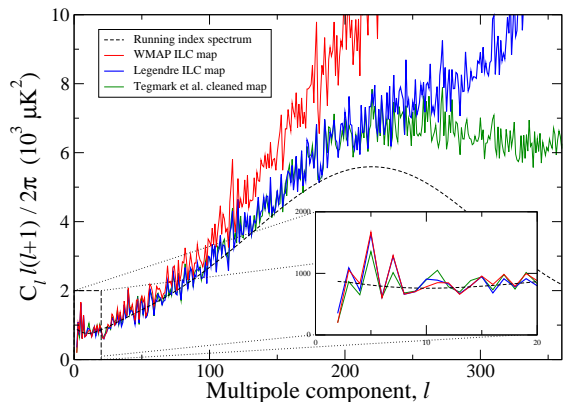


FIG. 4.— Comparison of the full sky power spectra of the WILC map (red), the LILC map (blue) and the TCM (green). Notice the excellent agreement between the two latter spectra up to  $l \approx 200$ , whereas the WILC spectrum departs from the other two already at  $l \approx 50$ .

contrary is true: by computing the residual fractions of each foreground in the high-latitude region as described in the previous section, we find that our map actually has slightly more foreground residuals than the WILC; the fractional residual foreground levels in the high-latitude *WMAP* ILC Kp2 region of the LILC map are  $[-0.075, -0.037, 0.620]$ , while for the WILC map they are  $[-0.033, -0.014, 0.415]$ <sup>8</sup>.

As noted in the previous section, the amount of residual dust is high in the ILC maps – the method is able to remove only half of the dust present in the W-band, where the dust is the dominant foreground. This result is thus in excellent agreement with the findings presented by Naselsky et al. (2003), which concludes that the cleaned maps contain residual foregrounds which mainly originate from the W-band.

#### 4.1. Quadrant and hemisphere weights

As pointed out earlier, one of the major weaknesses of the ILC method is its inability to handle spatial variations in the spectral indices of the foregrounds. To remedy this weakness Bennett et al. (2003b) divided the sky into 12 disjoint regions, and computed one set of weights

for each region. Out of those 12 regions, 11 lie within the Kp2 Galactic plane, while the rest of sky was treated as one single region. In light of the asymmetries recently reported by Eriksen et al. (2004a), we have partitioned the high-latitude sky yet further, and subsequently computed weights for the Galactic hemispheres and quadrants individually. The results from these computations are shown in Table 3.

We first consider the quadrant numbers (quadrants are defined by the standard Galactic reference system.) While the NW, NE and SW quadrant numbers are approximately internally consistent, the SE quadrant stands out in the Q and V bands. Thus, these numbers both support and ask question of the findings in Eriksen et al. (2004a). Certainly, the earlier results are supported in the sense that there is an asymmetry in the *WMAP* data, possibly marginally aligned from north-west to south-east. However, large differences in the weight coefficients would be interpreted most naturally in terms of variations of the noise and foreground properties, in apparent contradiction to the frequency independence demonstrated both by Eriksen et al. (2004a) and Eriksen et al. (2004b). Further investigation is certainly warranted, but it may yet be that foregrounds could play a role in explaining the observed asymmetries.

Unfortunately, it is difficult to assess the significance of the variations in Table 3 properly, but we can make a few rough estimates. We have generated 1000 simulated realizations, and computed quadrant weights as described above for each of these. Then, for each realization we find the maximum absolute difference between any two quadrants, for each frequency. The results from this exercise are summarized in Table 4, in terms of the mean, the standard deviation and the maximum value found in the simulations. Note that these numbers are only meant to give a rough idea of the shape of the distributions, and not for setting confidence levels – the distributions are non-Gaussian, and counting standard deviations is therefore meaningless. Nevertheless, it is obvious that the quadrant differences observed in the true *WMAP* data are inconsistent with the adopted foreground model described by the combination of three templates and fixed spectral indexes, and as proposed by the *WMAP* team. The weights of the south-east quadrant are radically different from those of the other three in the Q- and V-bands; the maximum difference found in the simulations in the V-band is about 80% that of the observed data. Whether this indicates a real foreground-

<sup>8</sup> Note that these observed fractions are in good agreement with the simulated values presented in Table 1. This supports our contention that the simulations mimic the true sky quite well at high latitudes.

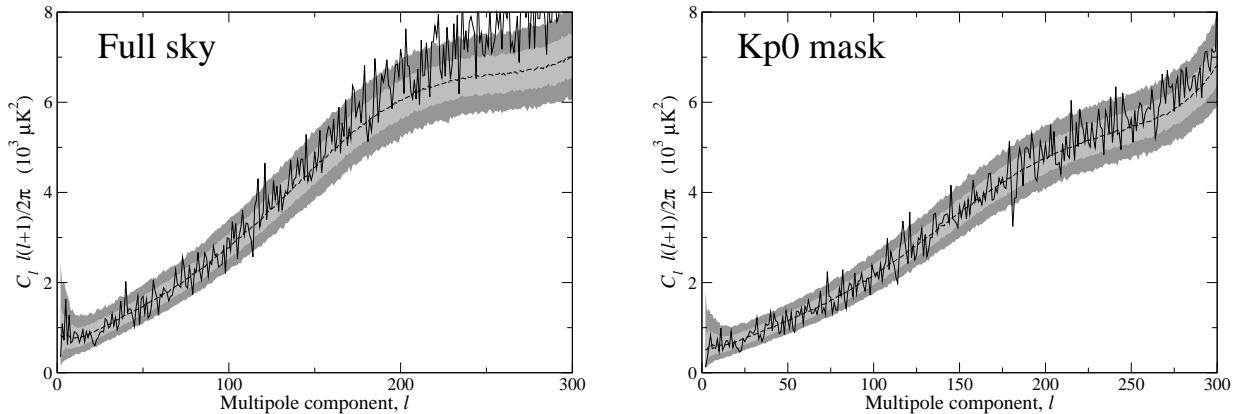


FIG. 5.— Comparison of the observed LILC power spectrum to the simulated spectrum. The gray bands correspond to 1 and  $2\sigma$  confidence bands, estimated from 1000 Monte Carlo simulations. The left panel shows the spectrum computed over the full sky, and the right panel shows the pseudo-spectrum of the maps when the Kp0 mask is applied.

TABLE 3. HEMISPHERE AND QUADRANT WEIGHTS

Region	K band	Ka band	Q band	V band	W band
Full sky	-0.19401	0.14004	0.07702	0.61214	0.36480
Northern hemisphere	-0.20611	0.14837	0.13262	0.55371	0.37140
Southern hemisphere	-0.18015	0.12169	0.03213	0.66930	0.35703
North-west quadrant	-0.19451	0.13659	0.09579	0.56725	0.39489
North-east quadrant	-0.24447	0.21397	0.20529	0.53331	0.29190
South-west quadrant	-0.19393	0.07268	0.26102	0.39229	0.46793
South-east quadrant	-0.16324	0.17738	-0.23334	1.01469	0.20451

NOTE. — Weights computed from Galactic hemispheres and quadrants outside the Kp2 mask.

TABLE 4. MAXIMUM ABSOLUTE QUADRANT WEIGHT DIFFERENCES

Frequency	Mean	Std.dev.	Max	WMAP
K-band	0.064	0.028	0.181	0.081
Ka-band	0.165	0.073	0.459	0.141
Q-band	0.169	0.074	0.505	0.494
V-band	0.157	0.071	0.502	0.622
W-band	0.179	0.082	0.496	0.263

NOTE. — The distribution of maximum absolute weight differences between any two Galactic quadrants, as computed from 1000 simulations. The observed *WMAP* values are shown in the right-most column.

or noise-related problem in the south-eastern quadrant is not clear from this analysis, but it does question the validity of treating the entire high-latitude sky as one single region.

The hemisphere results of Table 3 are by no means as decisive as the quadrant results, as the weights are more or less consistent with each other. However, this may very well be a coincidence; the internal variations between the north-west and north-east quadrants are much smaller than between the south-west and south-east quadrants, and yet, the two corresponding averages are rather similar.

## 5. IMPLICATIONS FOR AND STABILITY OF THE LARGE-SCALE MODES

TABLE 5. QUADRUPOLE AMPLITUDES

Measurement	$\delta T_2^2 (\mu K^2)$	p-value
Best-fit running index spectrum	869.7	
Hinshaw et al. cut sky	123.4	0.018
WMAP ILC map all sky	195.1	0.048
Tegmark et al.	201.6	0.051
Legendre ILC map	350.6	0.153
Legendre ILC map (quadrants)	345.1	0.149

NOTE. — Results from the measurements of the quadrupole amplitude. The third column lists the probability of finding a lower quadrupole than that of the corresponding map, given the theoretical model value shown in the first row.

In this Section we consider what implications our new LILC map have for the current debate concerning the peculiarities seen at the very largest scales, in particular the questions of the seemingly low quadrupole, the planar octopole and the alignment between the two, and we establish the uncertainties connected to each of these measurements. For these studies we adopt the statistics of de Oliveira-Costa et al. (2003), and compute 1) the probability of finding a lower quadrupole moment than the observed one, given the best-fit *WMAP* spectrum, 2) the probability of finding such a strong alignment between the quadrupole and octopole and 3) the probability of finding such a planar octopole. We refer to de Oliveira-Costa et al. (2003) for details on how these probabilities are computed.

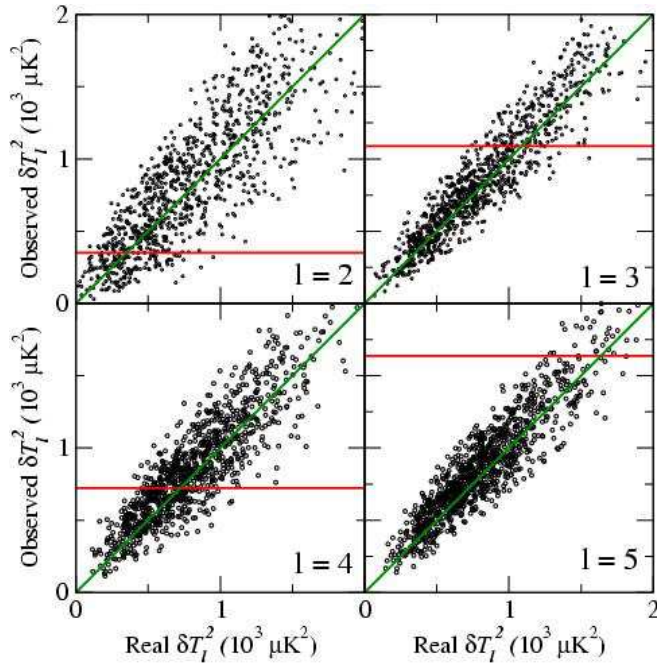


FIG. 6.— The observed multipole amplitude plotted against the true, foreground-free amplitude. The observed *WMAP* LILC value is marked by a horizontal red line, while the diagonal green line is meant to guide the eye only; in the case of perfect reconstruction, all dots would lie along this line. Note that there are generally more dots above the green line than below it, indicating that the ILC reconstructed spectra are slightly biased toward high values.

In Table 5 the amplitudes of the quadrupole moments are tabulated for four different maps: the WILC map, the TCM, our LILC map, and finally the LILC map for which the Kp2 region is divided into quadrants<sup>9</sup>. As we can see from the numbers in Table 5 the LILC quadrupole is significantly larger than those observed in the WILC map and the TCM map. In fact, according to our map, the CMB quadrupole is low only at the 1 to 7 level, or, in other words, it is in perfect agreement with the model. However, these measurements are associated with large uncertainties. It is true that there is no estimator induced variance in these measurements, as discussed by Efstathiou (2003), since we have access to the full sky, but we do know that the ILC method does not remove foregrounds perfectly in the presence of noise, and this obviously affects the large-scale modes.

To assess the uncertainties in these measurements we once again take advantage of our simulations, for which we know both the CMB component and the reconstructed map, and compare the first few low- $\ell$  amplitudes for each realization. These results are shown in Figure 6. Each black dot in these plots indicates the true vs. the reconstructed amplitude for one Monte Carlo realization, and in the limit of perfect reconstruction, they should therefore all lie along the green, diagonal line. However, noise and residual foregrounds do have a significant effect on these measurements, as seen by the considerable scatter in each panel.

<sup>9</sup> Note that some numbers in the tables are not identical to those presented by de Oliveira-Costa et al. (2003); some of their statistics were computed from  $N_{\text{side}} = 16$  maps, whereas we use  $N_{\text{side}} = 512$  in our computations.

The red horizontal lines indicate the LILC amplitudes, for which we obviously only know the reconstructed values. In the case of the much debated quadrupole amplitude, we see that the observed value of  $351 \mu\text{K}^2$  may in fact originate from a cosmological quadrupole of everything from  $130 \mu\text{K}^2$  to at least  $600 \mu\text{K}^2$ , and it is therefore difficult to assign a great deal of significance to this result. It is interesting to note that the WILC map, which contains less residual dust than our map, also features a lower quadrupole. The most appropriate conclusion to draw is that residual foregrounds can modify the quadrupole significantly, and it is important to propagate the uncertainties in foreground modeling into errors on such low order modes.

Given this fact, the approach taken by Efstathiou (2003) might prove more reliable if the foreground uncertainties are dominated by residuals in the Galactic plane. In this work, the low- $\ell$  power spectra of the WILC and the TCM maps are estimated on a cut sky (based on the *WMAP* Kp2 mask). The most likely quadrupole amplitudes are found to be  $223 \mu\text{K}^2$  and  $250 \mu\text{K}^2$ , respectively. Thus, a cut sky approach yields slightly higher values than the corresponding full-sky analysis does.

We now turn to the question of alignment between the quadrupole and the octopole. The results from these measurements are summarized in Table 6. In this case we find that the alignment is actually stronger in the LILC map than in the WILC and TCM maps, having a probability as low as 0.7%. But once again the associated variance is of great importance, and a scatter plot for these measurements are shown in Figure 7. While the 0.7% probability in itself is highly interesting, from the scatter evident in Figure 7 it is clear that the ILC method does not reproduce the phases of the low- $\ell$  modes accurately enough to justify a cosmological identification. Nevertheless, it is still worth noticing that there is a very small number of dots below the red line, and so the ILC method does not seem to systematically introduce couplings between the quadrupole and octopole modes.

Given that the LILC map contains more residual dust than the WILC and TCM maps and also features a stronger alignment between the quadrupole and the octopole, one may suspect that the alignment is driven by the dust component. In order to study this possibility further, we generated a scatter plot of the alignment parameter  $t$  vs. the residual dust level  $f_{\text{dust}}$ , looking for possible correlations. However, no such correlations were found, either for dust or for the two other foreground components. It is therefore difficult to conclude that the alignment is a direct result of residual foregrounds.

Finally, in Table 7 we show results from the planarity measurements of the  $\ell = 3, 5$  and  $6$  modes. As noted by de Oliveira-Costa et al. (2003), the octopole is planar roughly at the 1 to 10 level. Of course, this result is not very spectacular on its own, but nevertheless worth pointing out. However, it is also that the  $\ell = 6$  mode is rather planar, at the 98% level, and further, the  $\ell = 5$  mode is quite spherical symmetric, with only 5 – 10% of the simulations being less planar. The  $\ell = 4$  mode appears random in all respects. It is once again difficult to conclude whether any of these findings are significant, but they should be investigated in more detail in future, more sensitive analyses. Scatter plots of the planariness

TABLE 6. ALIGNMENT OF THE QUADRUPOLE AND THE OCTOPOLE

Measurement	$l_2$	$b_2$	$l_3$	$b_3$	Angle	$ \mathbf{n}_2 \cdot \mathbf{n}_3 $
WMAP ILC map all sky	278°	69°	236°	63°	12°	0.955
Tegmark et al.	258°	59°	238°	62°	10°	0.984
Legendre ILC map	247°	62°	233°	63°	7°	0.993
Legendre ILC map (quadrants)	245°	61°	231°	63°	7°	0.992

NOTE. — Results from measurements of the position of the preferred directions of the quadrupole and octopole moments (denoted by Galactic longitude and latitude), and the alignment between these. The right-most column lists the probability of finding a weaker alignment between the quadrupole and octopole directions.

TABLE 7. PLANARITY OF A FEW MULTIPOLES

Data set	$\ell = 3$		$\ell = 5$		$\ell = 6$	
	$t$	$P$	$t$	$P$	$t$	$P$
WMAP ILC map	0.930	0.124	0.338	0.891	0.768	0.028
Tegmark et al.	0.941	0.096	0.197	0.959	0.778	0.023
Legendre ILC map	0.933	0.116	0.309	0.910	0.805	0.014
Legendre ILC map (quadrants)	0.948	0.082	0.305	0.912	0.793	0.018

NOTE. — Results from measurements of the degree of planarity of the three multipoles,  $\ell = 3, 5, 6$ . The left column in each section shows how much of the total power in the mode is attributable to the  $a_{\ell l}$  component, as measured in a coordinate system in which the preferred direction is defined to be the  $z$ -axis. The right column shows the probability of finding a more planar multipole, as compared to an ensemble of 10 000 Gaussian simulations.

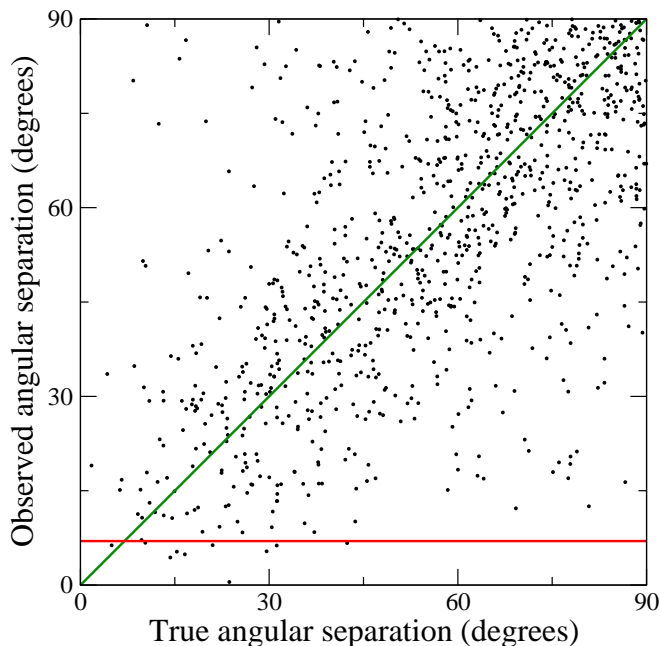


FIG. 7.— The observed angular separation between the preferred quadrupole direction,  $\mathbf{n}_2$ , and the preferred octopole direction,  $\mathbf{n}_3$ , plotted against the true, foreground-free separation. The symbols have the same meanings as in Figure 6.

measurements are shown in Figure 8, and a few low- $\ell$  modes are shown in Figure 9.

The main conclusion we draw from these calculations, however, is that residual foregrounds in the Galactic plane do produce significantly different low- $\ell$ -modes, and different foreground correction methods yield different results. Consequently, strong statements on the probability of finding such unlikely configurations seem somewhat premature – better measurements are needed before a cosmological connection may be made.

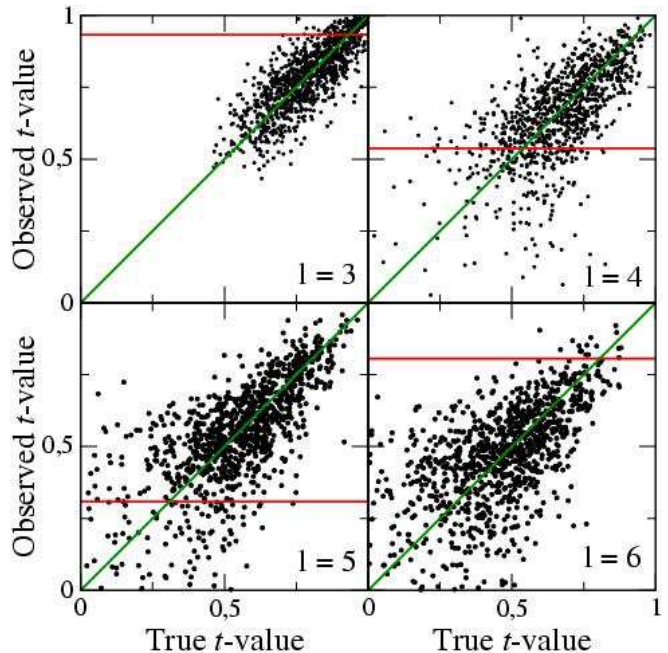


FIG. 8.— The observed  $t$ -value plotted against the true, foreground-free  $t$ -value. This parameter is defined as the fraction of the power attributable to the azimuthal component  $a_{\ell\ell}$  to the total power  $C_\ell$ , maximized over all reference frames. The symbols have the same meanings as in Figure 6.

## 6. CONCLUSIONS

The main goal of this paper was to study whether the ILC method is able to yield cosmologically useful maps, and if so, whether realistic simulations can be generated in reasonable time in order to calibrate the uncertainties associated with the use of such a map. The results presented earlier suggest a cautiously positive conclusion – the ILC method does have the capability of producing

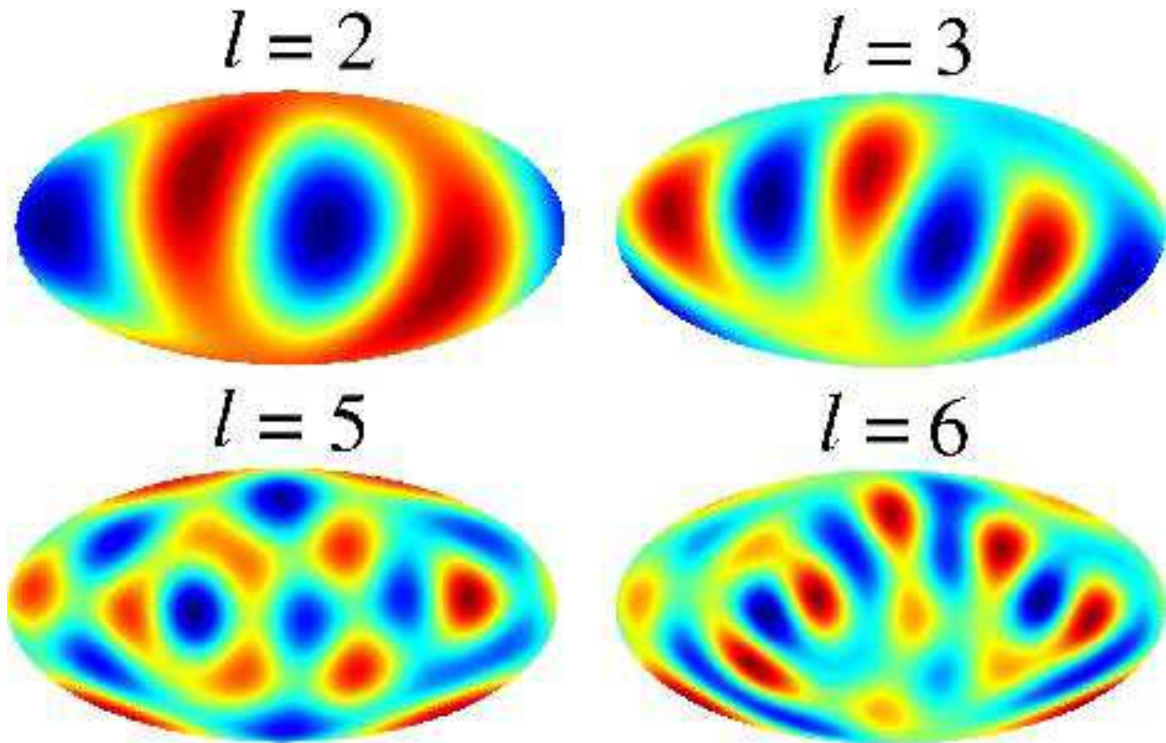


FIG. 9.— Four peculiar low- $\ell$  modes, computed from the LILC map. The preferred directions of the quadrupole and the octopoles are strongly aligned, the  $\ell = 5$  mode is spherically symmetric, and the  $\ell = 6$  mode is planar.

relatively clean CMB maps without the use of external templates. Nevertheless, great care should be taken in the practical implementation of the method (e.g. the proper definition of the individual regions is a crucial step), and beyond this one needs to be highly aware of its limitations.

On a more detailed level, we derived the equations for the ILC weights based on Lagrange multipliers, which were also discussed by Tegmark (1998). While a non-linear search algorithm is based on iterations, this method solves one single linear system of equations, and is therefore much faster. This is important when generating Monte Carlo simulations. Subsequently, we discussed how to produce realistic simulations of the ILC map, and used these simulations to study the properties of the method itself, with particular emphasis on the sensitivity to noise and sky cuts.

The method was applied to the real *WMAP* data, and the resultant LILC map was determined to have properties similar to the TCM map, but somewhat different from the official WILC map. We also computed ILC weights for four quadrants of the sky, and found that the south-eastern Galactic quadrant has significantly different properties than the other three, possibly shedding new light on the asymmetry issue discussed by Eriksen et al. (2004a).

Finally, as a comment to the on-going debate on the nature of the large-angular scale anisotropy, we investigated the implications of the LILC map to estimates of the quadrupole and octopole modes, and found that the new quadrupole moment increases from  $195 \mu\text{K}$  to  $351 \mu\text{K}$ , which is a perfectly acceptable amplitude compared to the best-fit spectrum. However, the alignment between

the quadrupole and the octopole is stronger in our map than in the WILC and the TCM. More importantly, it appears that the variance in these measurements is too large to draw meaningful cosmological conclusions at this point. The impact of residual foregrounds must be better understood and quantified in terms of the error budget.

As much potential as the ILC method shows, one may question whether the minimum variance criterion in itself is a meaningful measure of performance. As we have seen, this criterion implies a trade-off between suppressing noise and foregrounds, and moderate levels of foregrounds are often accepted in order to suppress noise. For most practical cosmological analyses this is not likely to be acceptable; noise is more easily quantified than residual foregrounds.

Note therefore that although we do provide a copy of the LILC map at HKE's home page<sup>10</sup>, we strongly advise against using it for purposes beyond visual presentation, for which, of course, the official WILC map is perfectly acceptable.

We thank Gary Hinshaw and Max Tegmark for useful discussions, and acknowledge use of the HEALPix<sup>11</sup> software (Górski, Hivon & Wandelt 1998) and analysis package for deriving the results in this paper. We also acknowledge use of the Legacy Archive for Microwave Background Data Analysis (LAMBDA). H. K. E. and P. B. L. acknowledge financial support from the Research Council of Norway, including a Ph. D. studentship for H. K. E. This work has also received support from The Re-

<sup>10</sup> [http://www.astro.uio.no/~hke/cmbdata/WMAP\\_ILC\\_lagrange.fits](http://www.astro.uio.no/~hke/cmbdata/WMAP_ILC_lagrange.fits)

<sup>11</sup> <http://www.eso.org/science/healpix/>

search Council of Norway (Programme for Supercomputing) through a grant of computing time. This work was partially performed at the Jet Propulsion Laboratory,

California Institute of Technology, under a contract with the National Aeronautics and Space Administration.

#### REFERENCES

- Banday, A. J., & Wolfendale, A. W. 1991, *MNRAS*, 248, 705  
 Bennett, C. L. et al. 2003a, *ApJS*, 148, 1  
 Bennett, C. L. et al. 2003b, *ApJS*, 148, 97  
 Brandt, W. N., Lawrence, C. R., Readhead, A. C. S., Pakianathan, J. N., & Fiola, T. M. 1994, *ApJ*, 424, 1  
 Chiang, L.-Y., Naselsky, P. D., Verkhodanov, O. V., & Way, M. J. 2003, *ApJ*, 590, 65  
 Coles, P., Dineen, P., Earl, J., & Wright, D. 2003, *MNRAS*, in press (astro-ph/0310252)  
 Copi, C. J., Huterer, D., & Starkman, G. D. 2003, preprint (astro-ph/0310511)  
 de Oliveira-Costa, A., Tegmark, M., Zaldarriaga, M., & Hamilton, A. 2003, preprint (astro-ph/0307282)  
 Eriksen, H. K., Hansen, F. K., Banday, A. J., Górski, K. M. & Lilje, P. B. 2004a, *ApJ*, in press (astro-ph/0307507)  
 Eriksen, H. K., Novikov, D. I., Lilje, P. B., Banday, A. J., & Górski, K. M. 2004b, *ApJ*, submitted (astro-ph/0401276)  
 Efstathiou, G. 2003, *MNRAS*, submitted (astro-ph/0310207)  
 Finkbeiner, D. P. 2003, *ApJ*, in press (astro-ph/0311547)  
 Finkbeiner D.P., Davis M., & Schlegel D.J. 1999, *ApJ*, 524, 867  
 Haslam, C.G.T., Salter, C.J., Stoffel, H., & Wilson, W. 1982, *A&AS*, 47, 1  
 Górski, K. M., Hivon, E., & Wandelt, B. D., 1999, in *Evolution of Large-Scale Structure: from Recombination to Garching*, ed. A. J. Banday, R. K. Sheth, & L. N. da Costa (Garching, Germany: European Southern Observatory), 37  
 Lagache, G. 2003, *A&A*, 405, 813  
 Naselsky, P. D., Verkhodanov, O. V., Chiang, L.-Y., & Novikov, I. D. 2003, *ApJ*, submitted, (astro-ph/0310235)  
 Park, C.-G. 2003, *MNRAS*, submitted (astro-ph/0307469)  
 Readhead, A. C. S., & Lawrence, C. R. 1992, *ARA&A*, 30, 653  
 Tegmark, M., & Efstathiou, G. 1996, *MNRAS*, 281, 1297  
 Tegmark, M. 1998, *ApJ*, 502, 1  
 Tegmark, M., Eisenstein, D. J., Hu, W., & de Oliveira-Costa, A. 2000, *ApJ*, 530, 133  
 Tegmark, M., de Oliveira-Costa, A., & Hamilton, A. J. 2003, *Phys. Rev. D*, 68, 123523  
 Vielva, P., Martínez-González, E., Barreiro, R. B., Sanz, J. L., & Cayón, L. 2003, preprint, (astro-ph/0310273)

#### APPENDIX

##### COMPUTING THE ILC WEIGHTS BY LAGRANGE MULTIPLIERS

In this appendix we describe how to compute the ILC weights both efficiently and accurately by means of Lagrange multipliers. Bennett et al. (2003b) do not specify how they carry out the minimization of Equation 4 in practice, other than stating that the minimum is found through a non-linear search. Thus, it is difficult to assess the accuracy of the final results they quote, as non-linear searches can often be plagued by convergence issues. However, again we remind the reader that the *WMAP* team only intended their ILC map to be used for visualization purposes, and obtaining high accuracy was therefore of little importance. Our goal, however, was to study whether this method may actually be used for cosmological purposes, as a credible alternative to the template correction method. In addition, Monte Carlo simulations was needed to fully account for the statistical noise properties of the method, therefore computational speed was a driving concern.

Recall that the problem is to minimize the variance of a linear weighted sum over  $k$  frequency maps, as given in Equation 4, under the constraint that the sum of weights equals unity. This latter constraint guarantees a correct response to the CMB component, while minimizing the variance suppresses residuals.

Let us start by writing the variance of the final map out explicitly,

$$\begin{aligned}
 \text{Var}(T) &= \langle T^2 \rangle - \langle T \rangle^2 \\
 &= \frac{1}{N_{\text{pix}}} \sum_{p=1}^{N_{\text{pix}}} \left[ \sum_{i=1}^k w_i T^i(p) \right]^2 - \left[ \frac{1}{N_{\text{pix}}} \sum_{p=1}^{N_{\text{pix}}} \left( \sum_{i=1}^k w_i T^i(p) \right) \right]^2 \\
 &= \sum_{i=1}^k \sum_{j=1}^k w_i w_j \left[ \frac{1}{N_{\text{pix}}} \sum_{p=1}^{N_{\text{pix}}} T^i(p) T^j(p) \right] - \left[ \sum_{i=1}^k w_{n,i} \left( \frac{1}{N_{\text{pix}}} \sum_{p=1}^{N_{\text{pix}}} T^i(p) \right) \right]^2 \\
 &= \mathbf{w}^T \mathbf{A} \mathbf{w} - (\mathbf{w}^T \mathbf{t})^2,
 \end{aligned} \tag{A1}$$

where  $\mathbf{w} = (w_1, \dots, w_k)^T$ ,  $\mathbf{t} = (t_1, \dots, t_k)^T$  and

$$t_i = \frac{1}{N_{\text{pix}}} \sum_{p=1}^{N_{\text{pix}}} T^i(p). \tag{A2}$$

The matrix  $\mathbf{A}$  is defined by

$$A_{ij} = \frac{1}{N_{\text{pix}}} \sum_{p=1}^{N_{\text{pix}}} T^i(p) T^j(p). \tag{A3}$$

Thus, the problem is simply to minimize a quadratic form, subject to the constraint given by Equation 2, a task which is most conveniently solved by Lagrange multipliers. Let us restate the problem slightly. First, we seek to minimize the following function,

$$f(\mathbf{w}) = \mathbf{w}^T \mathbf{A} \mathbf{w} - (\mathbf{w}^T \mathbf{t})^2 \tag{A4}$$

under the constraint

$$g(\mathbf{w}) = \sum_{i=1}^k w_i = 1. \quad (\text{A5})$$

In such cases the method of Lagrange multipliers tells us to look among those points,  $\mathbf{w}_0$ , which satisfies the following relation,

$$\nabla f(\mathbf{w}_0) = \lambda \nabla g(\mathbf{w}_0), \quad (\text{A6})$$

where  $\lambda$  is an arbitrary constant. In other words, the extrema of  $f$ , subject to the constraint,  $g = 1$ , are just those points at which the gradients of  $f$  and  $g$  are parallel.

The partial derivatives of our function,  $f$ , are easily computed from Equation A4, and can be written on the following form,

$$\frac{\partial f}{\partial w_i} = 2 \sum_{j=1}^k A_{ij} w_j - 2t_i \sum_{j=1}^k w_j t_j. \quad (\text{A7})$$

The partial derivatives of  $g$  are obviously just unity.

Thus, the extrema of  $f$  are found by simultaneously solving the system of  $k$  derivative equations given by Equation A6, and the constraint in Equation 2:

$$\begin{bmatrix} \mathbf{B} & -\mathbf{1} \\ \mathbf{1}^T & 0 \end{bmatrix} \begin{bmatrix} \mathbf{w} \\ \lambda \end{bmatrix} = \begin{bmatrix} \mathbf{0} \\ 1 \end{bmatrix}, \quad (\text{A8})$$

where

$$B_{ij} = 2(A_{ij} - t_i t_j). \quad (\text{A9})$$